
Experimental study of coherent flow structures past a wall-mounted square cylinder

Ikhennicheu Maria ^{1,*}, Germain Gregory ¹, Druault Philippe ², Gaurier Benoit ¹

¹ Ifremer, Marine Structure Laboratory, 150 Quai Gambetta 62200 Boulogne sur Mer, France

² Sorbonne Université, UPMC Univ Paris 06, CNRS, UMR 7190, Institut Jean Le Rond d'Alembert, F-75005, Paris, France

* Corresponding author : Maria Ikhennicheu, email address : maria.ikhennicheu@ifremer.fr

Abstract :

In high flow velocity areas like those suitable for tidal applications, turbulence intensity is high and flow variations may have a major impact on tidal turbines behaviour. Large boils that can be observed at the sea surface are emitted from the sea floor and may interact with the tidal turbines. These boils have then to be characterized. The Reynolds number, based on the rugosity height and the mean flow velocity, is rather high in this context: $Re \approx 2.5 \cdot 10^7$. For that purpose, experiments are carried out in a flume tank with Re as high as achievable in Froude similitude (in the tank: $Re \approx 2.5 \cdot 10^5$ and $Fr \approx 0.23$) in order to study coherent flow structures emitted behind seabed obstacles. The obstacle is here a canonical square wall-mounted cylinder chosen to be representative of specific in-situ bathymetric variations. Using PIV and LDV measurements, the flow past the cylinder is investigated. Using a POD filter, large coherent structures are identified and their trajectories are analysed. By means of a Lamb-Oseen profile approximation, properties of these structures are determined. The formation mechanism of such structures is discussed in this paper and their behaviour is characterized. It is assumed that vortices periodically shed from the obstacle interact and generate hairpin structures.

Highlights

► Experimental study of coherent flow structures past a wall-mounted square cylinder. ► Tests are carried out on a wall-mounted cylinder representative of seabed elements, in Froude similitude with high Reynolds number. ► PIV measurements are performed in vertical measurement planes and spatial analyses are performed. ► POD analysis and center detection allow to study the vortices behaviour.

Keywords : Turbulence, Experimental trials, Wall-mounted cylinder, PIV, LDV, POD, Lamb-Oseen

1. Introduction

Industrial projects have started to emerge in tidal energy harvesting. There is a strong tidal potential in Europe and over 25% of the European potential is located in French waters [EDF (2010)]. The area of interest is the Alderney Race that presents currents up to $U_{insitu} = 5m/s$. *In-situ*, strong velocity variations exist [Myers and Bahaj (2005)]. Such variations are causing a high turbulence rate in the water column. Some turbulent events can sometimes rise up to the surface and erupt to create a boil. Turbulence can have a major impact on the tidal turbines behaviour, on their production [Duràn Medina et al. (2017)] and on the structural fatigue [Mycek et al. (2014)]. Before trying to reproduce complex bathymetric structures, we chose to introduce the topic by studying elementary obstacles representative of real life condition: *i.e.* with an aspect ratio ($A_R = \text{Width}/\text{Height}$) of the magnitude of the mean bathymetry variations encountered between France and Alderney. Surveys performed in this area give access to the bathymetry (see Fig.1) showing an average depth variation of $H_{insitu} = 5m$.

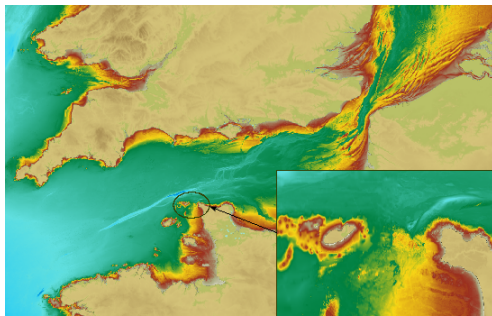


Figure 1: Bathymetry of the English Channel with a zoom of the Alderney Race area [SHOM (2015)].

Some bathymetry variations have been represented using elementary elements like wall-mounted cubes and an inclined floor representing smooth depth variations [Ikhennicheu et al. (2018a)]. The wake past a wall-mounted cube has been described and results show that the addition of an inclined floor downstream of the cube impules turbulent structures higher than the simple floor translation. However, the floor inclination does not have an impact on the nature of turbulent structures emitted from the obstacle wake. The aspect ratio impact on the wake development has been investigated in [Ikhennicheu et al. (2018b)], showing that for an aspect ratio 7 times supe-

rior, the recirculation length triples.

The matter of interest of this work is the development of the wake and the analysis of turbulent structures past large A_R obstacles. The case of $A_R = \infty$ is a classical example of a 2D obstacle in the literature. Among the firsts to ever characterize the flow past a 2D block (=rib), [Castro (1979)] characterized its wake in a flow at $Re = 1.5 \times 10^4$. More recently, [Liu et al. (2008)] carried out experiments on a rib in a turbulent flow for $Re = 1.3 \times 10^4$. They give a detailed explanation of the intermittency aspect of the reattachment of the recirculation region. They also found that at $x/H = 15.75$ in the obstacle wake, the streamwise velocity is not fully recovered, illustrating the wake extension past larger A_R obstacles. Indeed, at this location behind a 3D wall-mounted cube [Hearst et al. (2016)], the wake of the obstacle is fully dissipated. Finally, the experimental works of [Wang et al. (2009)] offer a topology of the fluid past a rib at $Re = 2.2 \times 10^4$. Detailed investigation on the turbulent organisation past a vertical cylinder can be found in the studies of [Sattari et al. (2012)] although different mechanism are expected for a horizontal cylinder. These studies on 2D ribs are completed by numerical works such as the one of [Panigrahi and Acharya (2004)] who simulated a turbulent flow at $Re = 1.4 \times 10^4$ on 2D square ribs. For obstacles with high A_R , the two ends of the horseshoe vortex are farther apart and have smaller influence on the middle region of the wake, unlike for small A_R obstacles where they interact and cause the 3D behaviour of the wake. Intermediate A_R were experimentally studied by [Martinuzzi and Tropea (1993)]. They found that for $A_R \geq 6$, the recirculation region downstream of the cube switches from a 3D aspect to a nominally 2D aspect. The main differences between 2D and 3D square obstacles are extensively described by [Schofield and Logan (1990)].

Few of the studies exposed in this bibliographic review present cases with $Re > 10^5$. It is generally assumed that, for $Re > 4 \times 10^4$, the flow achieves a certain Reynolds number independency as found by [Castro and Robins (1977)]. However, that conclusion has been questioned in [Lim et al. (2007)] where it is explained that for vortex-dominated flows, mean flow is likely to be Re-dependant. The Reynolds number, based on H_{insitu} and U_{insitu} is substantially high: $Re_{insitu} = H_{insitu}U_{insitu}/\nu = 2.5 \times 10^7$, with ν the kinematic viscosity of water. Hence, there is a necessity to extend the existing database for marine energy application through high Reynolds number experiments.

Few studies are lead on the far field of wide wall-mounted obstacles in a high Reynolds number flow and especially with a focus on the turbulent structures that are emitted from the wake. Large turbulent events can have a major impact on turbines [Mycek et al. (2014)], hence the need to investigate them. In many cases in the literature, coherent turbulent structures can be observed past an obstacle or in a turbulent boundary layer. One of the most extensive analysis of structures emitted from turbulent boundary layers is the work of [Adrian et al. (2000)]. They detailed the creation, detection and transport of hairpin structures in the flow. For wide square plates, the numerical study of [Diabil et al. (2017)] for $Re = 6.5 \times 10^3$ shows that Kelvin-Helmholtz vortices are shed from the upstream face of the obstacle. Periodically shed vortices create corotating pairs that lead to vortex pairing as described by the annual review of [Leweke et al. (2016)]. Their analysis uses a Lamb-Oseen model for vortex profile fitting as will be done here. [Müller and Gyr (1987)] demonstrate that these vortices interact or merge to create hairpin structures. These hairpins are sometimes called Kolk vortices in other studies [Best (2005b)]. Such structures are very energetic and can rise up to the surface to form a large boil [Best (2005a)]. [Volino et al. (2009)] studied coherent structures created over a rough bottom. They show that their size varies with the upstream flow conditions however the rising angle is conserved. [Sabatino and Rossmann (2016)] proposed tomographic PIV measurements of hairpin vortex developing in laminar boundary layers. They illustrate how hairpin vortices regenerate with the creation of secondary hairpin vortices. This kind of turbulent structures shall be characterized in order to predict their trajectory and frequency as well as the incoming velocity profile on tidal turbines.

In this paper, coherent structures developing from the wake of a wall-mounted cylinder representative of seabed element is studied. The experimental set up is first presented and test cases are detailed. Then, the characterization of the wake past the cylinder is carried out from experimental results in and out of the symmetry plane. Vortices are studied and a method to detect their centre and track their position is proposed. A Lamb-Oseen vortex approximation is proposed for the determination of the vortex properties. A temporal analysis is added to the turbulent structures analysis. Finally, a discussion on the turbulent organization formed in the obstacle wake is proposed.

2. Experimental set-up

The tests are carried out in the wave and current circulating flume tank of IFREMER located in Boulogne-sur-Mer (France) presented in Fig.2(a). The test section is: 18m long \times 4m wide \times 2m high. In this work, the three instantaneous velocity components are denoted (U, V, W) along the (X, Y, Z) directions respectively (Fig.2(b)). Each instantaneous velocity component is separated into a mean value and a fluctuating part according to the Reynolds decomposition: $U = \bar{U} + u'$, where an overbar indicates the time average. The incoming flow ($\bar{U}_\infty, \bar{V}_\infty, \bar{W}_\infty$) is assumed to be steady and constant. By means of a grid and a honeycomb (that acts as a flow straightener) placed at the inlet of the working section (see Fig.2(b)), a turbulent intensity of $I = 1.5\%$ is achieved for a flow velocity of 1m/s. Turbulence intensity I in the incoming flow is defined as follows:

$$I = 100 \sqrt{\frac{\frac{1}{3}(\overline{u'^2} + \overline{v'^2} + \overline{w'^2})}{\bar{U}_\infty^2 + \bar{V}_\infty^2 + \bar{W}_\infty^2}} \quad (1)$$

Table 1: *in-situ* and experimental conditions (1:20 scale).

	Scale	U_∞ [m/s]	Rugosity height H [m]	Depth D [m]	$Re = \frac{HU_\infty}{\nu}$	$Fr = \frac{U_\infty}{\sqrt{gD}}$
Alderney Race	1	5	5	40	2.5×10^7	0,25
Flume tank	1/20	1	0.25	2	2.5×10^5	0.23

The wall-mounted cylinder is chosen to be representative of real-life conditions. As there is no obstacle upstream of the cylinder: the upstream flow is a simple boundary layer developing over the tank floor. Hence the experimental set-up represents a bump considerably higher than its neighbours. To consider turbulent events interaction with the free surface, experiments shall be achieved in Froude similitude (see Table 1) where $Fr = \frac{U_\infty}{\sqrt{gD}}$, with g the gravity and D the tank depth. Furthermore, Reynolds number must be as high as achievable to be closer to real conditions. The obstacle of interest in this study is a wall-mounted cylinder of aspect ratio $A_R = \text{Width/Height} = 6$ represented in Fig.3. This element represents a key bathymetric element in the area of interest at a 1:20 scale (see Table 1). In the following study, non dimensional lengths are used for all parameters indexed by *: $x^* = x/H$, $y^* = y/H$, $z^* = z/H$ and $\delta^* = \delta/H$, with H the cylinder height ($H = 0.25$ m). At the obstacle position, the bound-

ary layer height δ^* is calculated as $\delta_{95}^* = z^*(\overline{U} = 0.95\overline{U}_\infty)$. It yields $\delta^* = 1.3$.

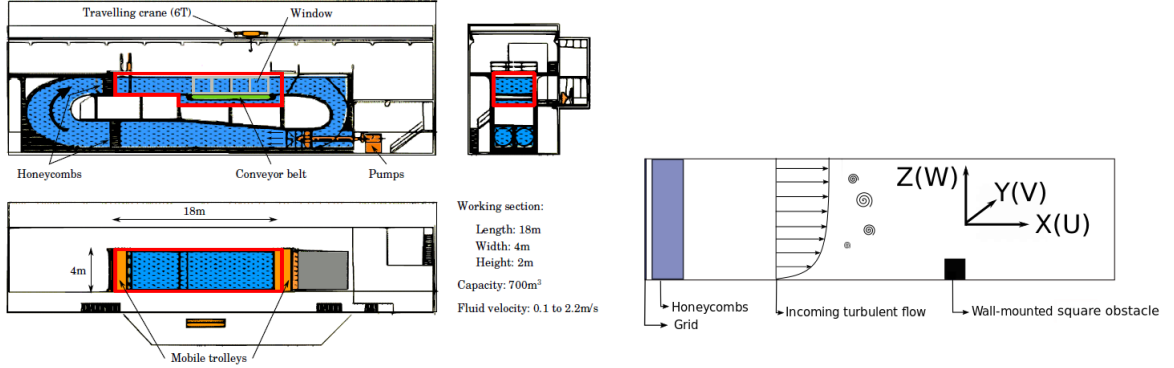


Figure 2: IFREMER Flume tank description and schematic view of the experimental set-up.

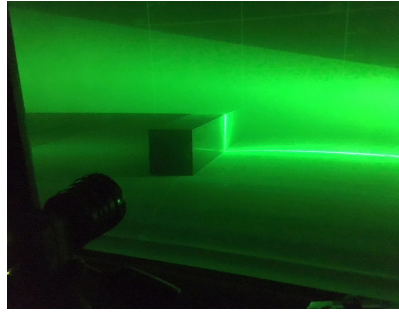


Figure 3: Cylinder during PIV measurements.

To characterize the flow, two Laser Velocimetry techniques are used: LDV (Laser Doppler Velocimetry) and PIV (Particle Image Velocimetry) (see Fig.3). Beforehand, the tank is seeded with $10 \mu\text{m}$ diameter silver coated glass micro-particles. For the PIV measurements, a Nd-YAG Laser GEMINI-LIKE is used: power is 200 mJ per probe and wavelength is 532 mm . The laser is synchronized with a Camera FLOWSENS EO-2M $1600\text{pix} \times 1200\text{pix}$ that makes double images with a time step of $1600 \mu\text{s}$. A particle is detected on 3 to 5 pixels. Cross-correlation peak intensity is between 0.3 and 0.8 and peak detectability (ratio of the tallest correlation peak and the second tallest correlation peak [Adrian and Westerweel (2011)]) is 8 in average. PIV acquisitions are made for 150s , hence 2250 double images are taken with a $15H_z$ acquisition frequency. The data are post processed with the software DYNAMIC STUDIO. The displacement of particles is calculated

using a Cross-Correlation on $32\text{pix} \times 32\text{pix}$ interrogation windows with 50% overlap [Meinhart et al. (1993)]. Outliers are replaced with the Universal Outlier Detection [Westerweel and Scarano (2005)]. Depending on the plane, from 1% to 13% of the total vectors number are substituted. Single-pass method is used as, in our case, multi-pass adaptive PIV leads to errors generating artefacts rather than improving resolution. PIV measurements are carried out at various transverse positions: $y^* = 0$, $y^* = 1$ and $y^* = 2$ (denoted y_0 , y_1 and y_2 respectively) summarized in Table 2 and represented in Fig.4(b). Fig.4(a) shows the 13 measurement planes carried out for each transverse position. In the tank, using a wide angle lens for a large surface detection, only vertical PIV measurement planes can be achieved. Hence, only 2D measurements of (U, W) will be performed in this study. The experimental set-up allows measurements for $z^* \in [0.5; 7]$. Fig.5 illustrates the post-processing steps applied in the plane y_0 : from the raw image to the Universal Outlier Detection (UOD). The Cross-Correlation (CC) results are obtained with a mask applied on the cylinder.

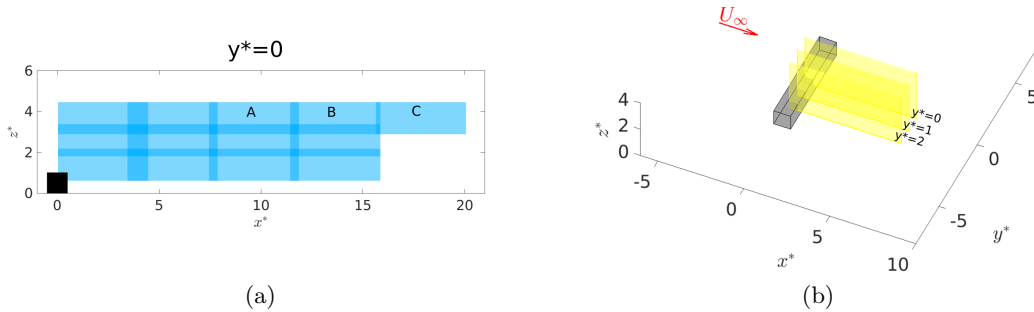


Figure 4: PIV measurement planes locations in the wake of a wall-mounted cylinder. Origin is taken at the middle of the bottom face of the cylinder.

Table 2: PIV measurement characteristics.

Plane	Field [pix ²]	Field [mm ²]	Spatial discretization [mm]
$y^* = 0$ (y_0)	1600×600	1153×430	11.6
$y^* = 1$ (y_1)	1600×600	1250×470	12.6
$y^* = 2$ (y_2)	1600×600	1360×510	13.7

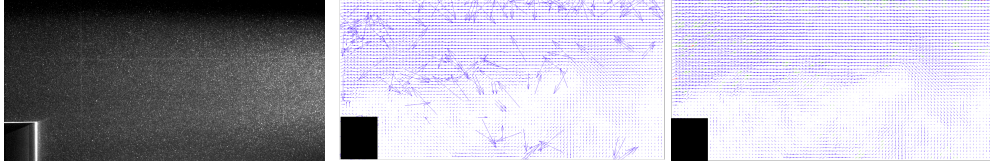


Figure 5: Post-processing illustration from the raw image (**left**) to the CC+UOD (**right**) (CC in the **middle**).

The LDV measurements are made using a 2D DANTEC FIBERFLOW system. The probe is positioned horizontally for (U, V) measurements at various streamwise positions along the Z axis. With LDV measurements, the acquisition frequency is not constant. It depends on the number of particles passing through the measurement volume. Then, a re-sampling is done in the post processing. Based on previous works performed in the tank [Duràn Medina et al. (2015)], the re-sampling is done using the mean sample rate of the measurements set considered. At a specific streamwise position, f_e varies from 70 to 270 H_z depending on the turbulent agitation.

Various sources of experimental errors can be identified. Positions fixed using the human eyes are considered to have a maximum error of 0.5 cm and 0.5° ; it is the case for the obstacle and the lasers positioning. Particles motion follows the Basset-Boussinesq-Oseen equation; for silver-covered glass particle, the response of particle is of 0.14 mm/s . The laser sheet induces a magnification that causes an error of 0.3% [Adrian and Westerweel (2011)]. Measurement standard deviation goes up to 0.1%. Calibration is achieved by the LDV manufacturer. Additionally, vibration of the LDV probe due to vortex induced vibration can induce an error up to ± 0.5 cm . PIV calibration is precise at 1 mm . The pixel size is added to the errors for PIV measurements. Hence, the errors on the results are of 2% and 2.6% for LDV and PIV respectively. A comparison is made in Fig.6 between PIV and LDV measurements in the symmetry plane showing a good coherency.

3. Characterization of the wake past the wall-mounted cylinder

Average velocity maps of \bar{U} and \bar{W} in plans y_0 , y_1 and y_2 are presented in Fig.7. In these figures, the classical behaviour of the flow past a wall-mounted element can be observed: the flow separates at the leading edges of the cylinder into the outer steady region and the recirculation area downstream of the cylinder. A shear layer develops in-between and then the flow

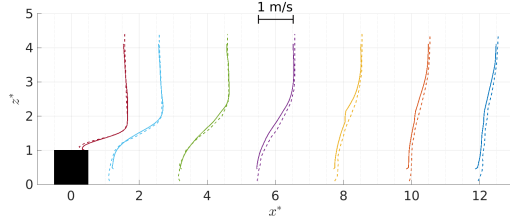


Figure 6: LDV measurements (dotted lines) and PIV measurement (full lines) \bar{U}/U_∞ profiles comparison in $y^* = 0$.

reattaches. The recirculation length downstream of the obstacle is evaluated for the 3 planes: $l_{y0}^* = 6$, $l_{y1}^* = 5.5$ and $l_{y2}^* = 4.5$. As expected, the apparition of 3D effects mainly impacts planes for $y > y1$: the l^* reduction between $y0$ and $y1$ is 8% and l^* reduction increases to 18% between $y1$ and $y2$. In [Martinuzzi and Tropea (1993)], at a similar Re and A_R , a recirculation length of $l^* = 5.7$ has been measured in the symmetry plane, which is close to our results. Maps of the average vertical velocity \bar{W} out of the symmetry plane indicate that the flow passing over the obstacle is similar in the 3 planes for $x^* < 2$. However, downstream of the cylinder, the flow is considerably redirected towards the floor for position $y2$ with a large and intense $\bar{W} < 0$ zone. In $y0$, the flow shows an area of $\bar{W} > 0$ beginning at $x^* = 6$ from the floor up to $z^* \sim 1$. The wake is impulsed towards the surface.

Fig.8(a) and 8(b) show that, in $y0$, the transverse component V is relatively unaffected by the cylinder wake. The velocity fluctuations at $z^* = 2$, indicates a large shear stress area for u' and w' that does not affect v' . At $z^* = 2$ for instance, values are $U/U_\infty = 0.64 \pm 0.2$, $V/U_\infty = 0.003 \pm 0.04$ and $W/U_\infty = -0.05 \pm 0.16$.

In order to better understand the development of the wake past the cylinder, average Reynolds shear stress $\tau_{uw} = \overline{u'w'}$ maps are plotted in Fig.9. Some areas suffer from the poor lightning and data in these area are not fully converged. However, it appears that the shear layer reduces faster for $y1$ compared to $y0$ although the global orientation is similar. In field $y2$, the shear layer length reduces by half and is reoriented towards the floor. Here the shear layer length is estimated as the length corresponding to the position at which $|\tau_{uw}/U_\infty^2| < 0.02$. This effect is also visible when comparing \bar{W} maps in Fig.7. In $x^* = 7$, the shear layer starts disappearing

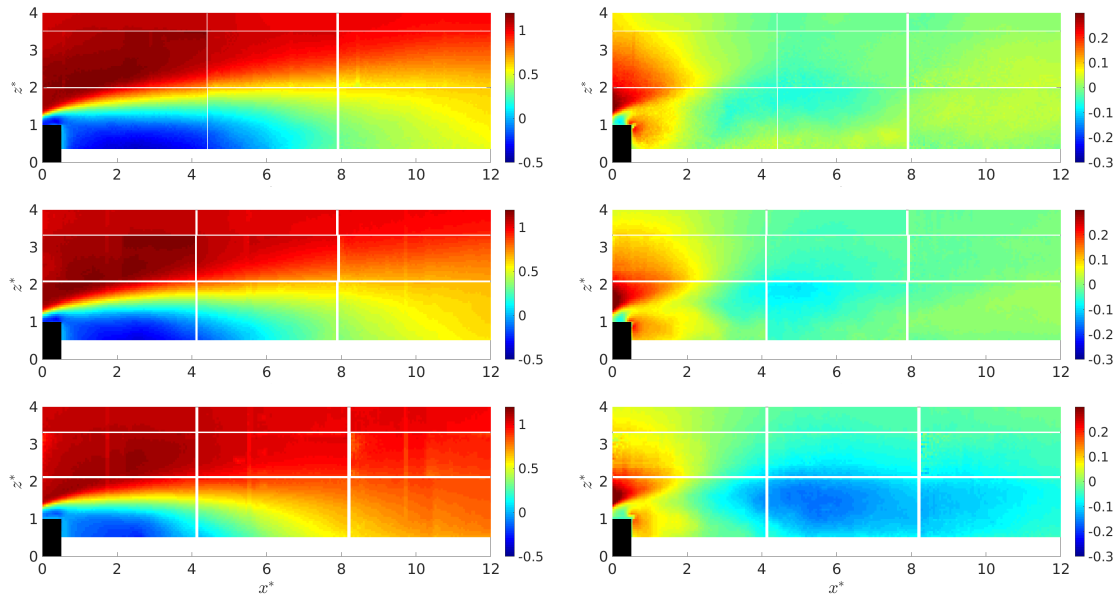


Figure 7: \bar{U}/U_∞ (left) and \bar{W}/U_∞ (right) maps in plane y_0 (top), y_1 (middle) and y_2 (bottom). White parts indicate the different PIV measurement planes separation.

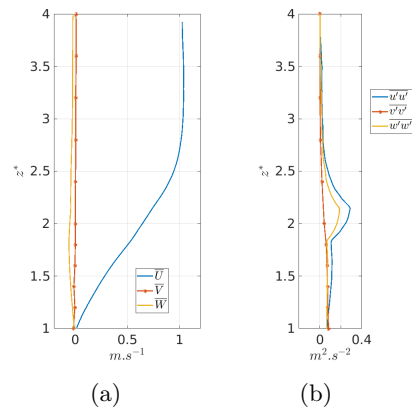


Figure 8: Average (left) and fluctuating (right) velocity profiles in $x^* = 5, y_0$. V is measured using LDV and (U, W) using PIV.

for y_2 but persists for the other two planes.

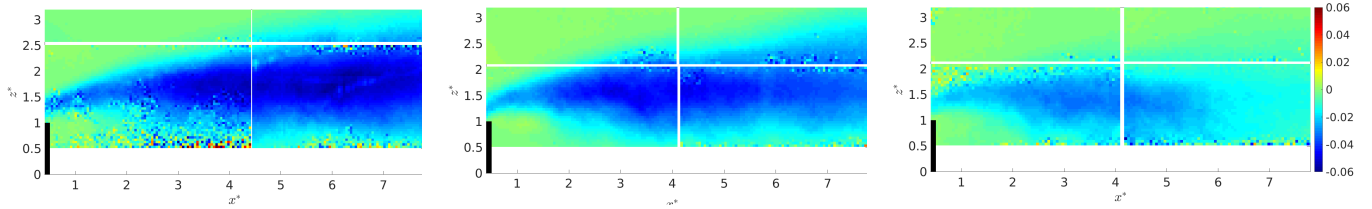


Figure 9: τ_{uw}/U_∞^2 maps in plane y_0 (left), y_1 (middle) and y_2 (right).

4. Turbulent structures dynamics

During the experiments performed for this study, large boils are observed at the tank free surface as illustrated in Fig.10 (taken $8m$ past the obstacle). Such events originate in the shear layer past the cylinder and rise up to the surface, located at $2 m$ from the bottom. These events are highly energetic with a $\sim 1 m$ diameter. It is the same kind of vortices that can be observed at the sea surface in the Alderney Race. These events evolving in the water column and carrying high velocity variations might have a strong impact on tidal turbines. Their investigation is detailed in this section in order to be able to quantify their effect on the flow impacting a potential turbine. In this part, POD (Proper Orthogonal Decomposition) is used as a filter on PIV measurement results in order to highlight the highest energetic structures and leave aside the non-coherent turbulent part. Then, based on the extracted energetic flow structures, a centre detection algorithm is implemented on POD filtered data in order to characterize the dynamic of turbulent events present in the flow. Structures properties are also investigated using a Lamb-Oseen vortex approximation.

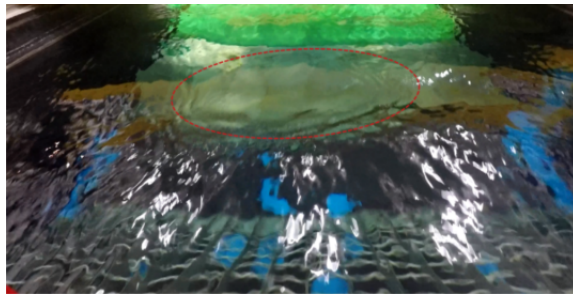


Figure 10: Picture of a boil of diameter $\sim 1m$ at the tank surface at $\sim 8m$ of a wall-mounted cylinder.

4.1. POD filter and vortex properties

4.1.1. POD filter

POD is an efficient and optimal mathematical tool to extract energetic coherent structures embedded in a turbulent flow. It was first introduced by [Lumley (1967)]. The snapshot version of POD [Sirovich (1987)] is used in the present work. Details of the implementation of POD technique applied to PIV database can be found in [Druault et al. (2005, 2012)]. Following previous works [Ikhennicheu et al. (2018a)], a vectorial POD is performed in this study. In order to determine the number of POD modes (N_{POD}) used to filter the large turbulent structures, the effect of POD filter on the fluctuating velocity field is investigated in Fig.11 during the passing of a vortex in plane B (see Fig.4). This specific vortex is selected because its centre position is in the middle of the plane and because there is no other vortex close by. In the raw field without filter, a vortex appears but its centre is difficult to properly position. With $N_{POD} \geq 20$, the POD filter is efficient although some turbulent noise is still present and that could hinder the centre detection. With $N_{POD} = 10$ rotating velocity is weaker since it is less energetic. Hence the required POD modes number lies between 10 and 20 which corresponds to between 69% and 76% of the total kinetic energy level. Arbitrary, it is chosen to take, in the following, 70% of the total kinetic energy for each measurement plane. For plane B, it corresponds to 13 modes.

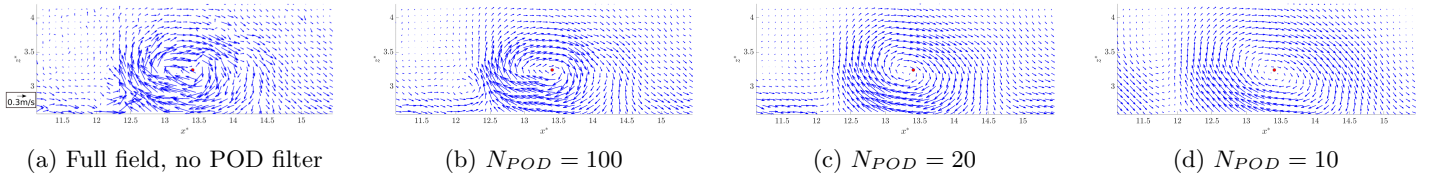


Figure 11: Effect of the POD modes number on the fluctuating velocity u' and w' field in the plane B (y_0).

4.1.2. Vortex properties

A centre detection algorithm, inspired by the method proposed by [Graftieaux et al. (2001)] and adapted for PIV measurements by [Druault et al. (2005)] is here considered. In each point M, the tangential fluctuating velocity V_θ is evaluated for the $2 \times 8 = 16$ neighbours as represented in Fig.12. If every V_θ around M has the same sign, a vortex centre is detected. A sensibility analysis allowed to fix 16 vortices to achieve a good centre detection. To

have trajectories long enough for statistic analysis, this study is restricted to trajectories detected on at least 7 temporally consecutive detected points, corresponding to a minimal detection time of $7 \times \Delta_t = 0.47 \text{ s}$. The centre detected with the algorithm is indicated with a red dot in Fig.13. The full trajectory obtained is represented in Fig.14.

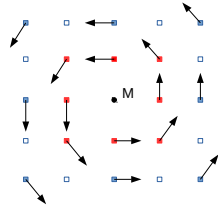


Figure 12: Schematic representation of vortex centre detection using tangential fluctuating velocities V_θ around a centre located in M for the $16 = 2 \times 8$ neighbours in red and blue.

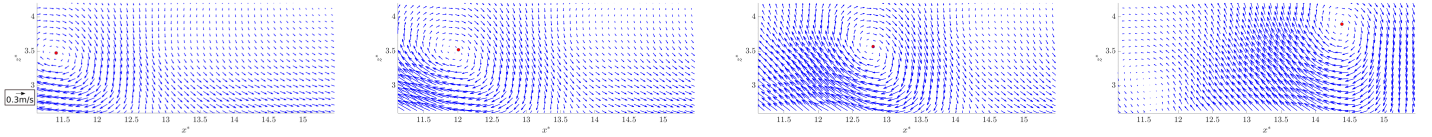


Figure 13: Vortex centre in plane B (y_0) from $t = 26s$ to $t = 27.5s$.

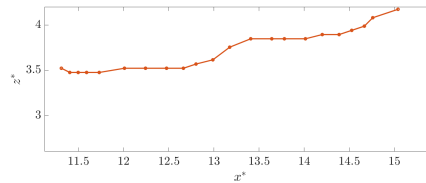
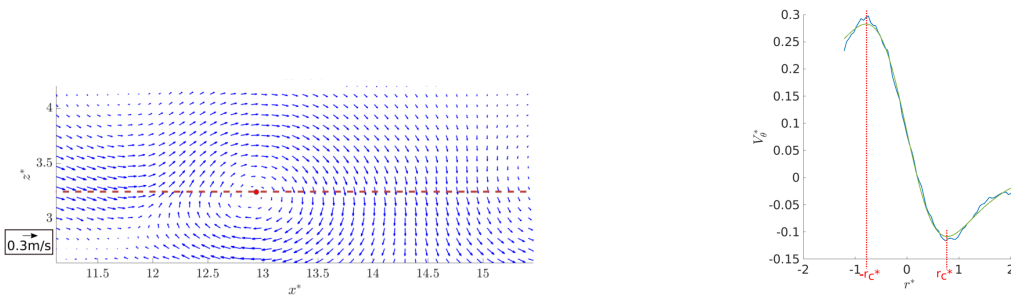


Figure 14: Trajectory of the vortex detected in Fig.13.

Following previous studies [Hamed et al. (2017); Leweke et al. (2016)] the head of vortices (supposed to be a hairpin vortex) detected in 2D PIV planes can be modelled thanks to a simplified Lamb-Oseen vortex model following [Moriconi (2009)]. Such vortex is defined by equation 2.

$$V_\theta(r) = \frac{\Gamma}{2\pi r} [1 - \exp(-\frac{r^2}{r_c^2})] \quad (2)$$

with Γ the circulation and r the radius, r_c is the vortex core size (see Fig.15(b)). Dimensionless values are used: $r_c^* = r_c/H$ and $\Gamma^* = \Gamma/(HU_\infty)$. Only vortices that are in the middle of the plane can be properly fitted since a sufficient quantity of data points is necessary. A vortex passing in the middle of plane B is chosen. Its tangential velocity V_θ is plotted with $r^* = r/H \in [-2; 2]$ and $\theta = 0^\circ$ (*i.e.* z^* constant) as illustrated in Fig.15(a). It is then fitted by a Lamb-Oseen profile in Fig.15(b).



(a) Velocity map with vortex centre detected (red dot). (b) POD filtered V_θ profile (blue) fitted with a Lamb-Oseen profile (green). Red dotted line indicates the altitude for V_θ profile. r_c^* (red) is the vortex radius.

Figure 15: Lamb-Oseen vortex approximation of a vortex passing in plane B (y_0), at $t = 58.4s$.

The Lamb-Oseen model is designed for circular symmetrical vortices. Due to a ratio between the size of the vortex and the height of the measurement plane close to 1, it is not possible to perform a Lamb-Oseen vortex approximation for $\theta = 0^\circ$ to $\theta = 90^\circ$ for all vortices to make sure the approximation is valid in every directions. It is only possible for some vortices that are located at mid-height of the plane. Fig.16 shows two cases of vortices for which the approximation is performed for $\theta = 0^\circ$ and $\theta = 90^\circ$. Most of the vortices are symmetrical, similar to the one on Fig.16(a). However, some vortices present an elliptical form which results in the non-identical profiles presented on Fig.16(b). More precisions on the specific case of elliptical vortices will be given later in the paper.

4.2. Analysis of the turbulent structures

The algorithm is applied to every PIV measurement planes. All the trajectories are gathered in Fig.17(a) for the plane y_0 . The top of the shear layer is determined from Fig.9 where $\tau_{uw} > -0.02$. This figure shows that vortices

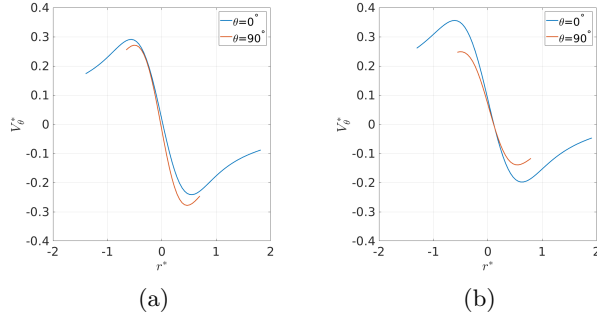
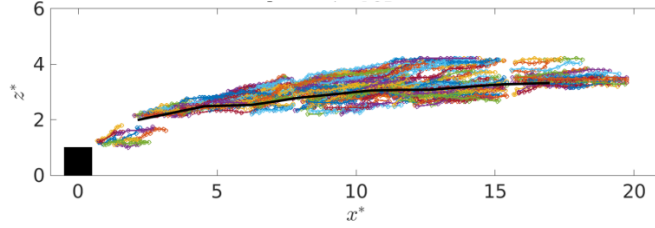


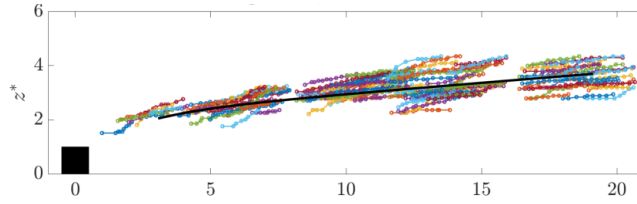
Figure 16: Tangential velocity V_θ^* profiles versus the radius r^* of Lamb-Oseen vortex approximation of vortices passing in plane B (y_0), at $t = 100s$ (a) and $t = 2.7s$ (b).

are generated in the beginning of the shear layer and are then emitted in the flow. Close to the obstacle (first PIV planes: $x^* < 4$), it is expected that trajectories detected are Kelvin-Helmholtz vortices. Higher in the water column and further in the flow, detected vortices are expected to resemble hairpin vortices. Trajectories are also presented in plane y_1 in Fig.17(b). Results are similar to those obtained for y_0 , while in y_2 , no vortices are detected. It is assumed that the same wide 3D structure is detected on both 2D planes (y_0 and y_1) as sections of a larger 3D structure, even if vortices detected in one plane are not linked with vortices detected in the contiguous plane. The 3D shape of the vortices is then contained in a $2H \times 3H \times 2H$ volume (x, y, z directions). The planes A, B and C contain the most vortices. They are also the most representative of the vortex behaviour since they are located just above the shear layer where turbulent structures are emitted. Fig.18 illustrates the trajectories detected for planes A, B and C. On plane A, trajectories are impulsed from the shear layer and oriented towards the surface with an angle of $\sim 9^\circ$. All trajectories are localized in the low part of the plane. Then, for planes B and C, trajectories appear more horizontal and more scattered. They are being dispersed and carried out by the flow. It is worth noticing that some trajectories in plane B (in bold in Fig.18(b)) are particularly oriented towards the surface. It is assumed that these are the trajectories of vortices that might erupt at the surface.

A linear interpolation is achieved on every trajectory in order to study the rising angle γ of each vortex. In average, the mean rising angle γ is found between 6° to 10° . It is substantially higher than the average rising angle of the shear layer, which is around 4° (see Fig.9(a)). There is a strong

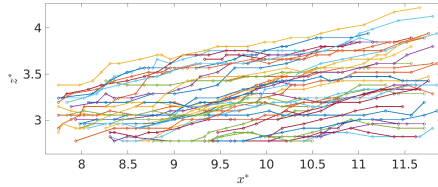


(a)

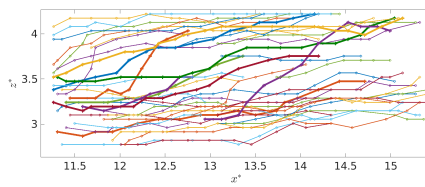


(b)

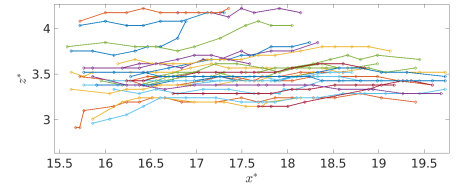
Figure 17: Vortices trajectories in y_0 (**top**) and y_1 (**bottom**) (black line: top of the shear layer).



(a) Plane A, 44 vortices detected



(b) Plane B, 45 vortices detected



(c) Plane C, 30 vortices detected

Figure 18: Vortex centre trajectories in y_0 .

dispersion of γ due to the large range of trajectory angles, however the average rising angle reduces when x^* increases. The discrepancy of rising angle results in figure 17 might be caused by 3D effects in the wake or by the unsteady interaction of emitted vortices with one another as explained by [Müller and Gyr (1987)]. The boil represented in Fig.10 corresponds to a rarely occurred event with an angle of 14° which is in the higher range of vortex trajectories. This indicates that some trajectories are particularly impulsed towards the surface compared to others. The low rising angle trajectories cannot be observed in the present set up since they would erupt downstream of the working section end (where the boil picture represented in Fig.10 is taken).

The approximation of the vortex fluctuating tangential velocity with a Lamb-Oseen profile is applied to vortices located in the middle of the measurement plane in order to have enough data points for profile fitting. The superposition of fitted profiles for plane C are plotted in Fig.19. This shows that the vortex profiles are generally symmetrical about their vertical axis. V_θ^* varies between $[-0.21; 0.25]$. Velocity profiles are slightly non-symmetrical about their horizontal axis. $|V_\theta^*|$ is larger upstream of the vortex centre, where its value is positive: it is connected to the rising vortices trajectory towards the free surface.

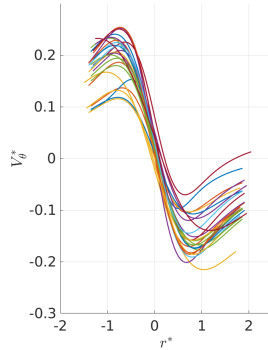


Figure 19: Tangential velocity V_θ^* profiles versus the radius r^* fitted with a Lamb-Oseen vortex for plane C in y_0 and centred at the inflection point (derivative maximum abscissa set to 0).

The radius (r_c^*) and the circulation (Γ^*) obtained with the Lamb-Oseen vortex approximation are presented in Table 3 for plane y_0 . The number of vortices that present enough data points for profile fitting is indicated compared to the total number of trajectories detected in the measurement plane. Standard deviation is around 25% on r_c^* but higher on Γ^* . Nevertheless, global behaviour can be drawn from these results. $|\Gamma^*|$ decreases when x^* increases and r_c does not vary significantly. Vortices that are emitted from the shear layer weaken due to dissipation effect. In average, vortices have a diameter of 0.30 m ($\sim H$) in the symmetry plane in the sense of the Lamb-Oseen vortex approximation. However, the vortices fluctuations themselves are present as long as $V_\theta > 0$ and in that perspective, the diameter of the vortex velocity perturbations is of the order of 1 m. The Lamb-Oseen modelling is also applied to y_1 vortices and averaged results are presented in table 3. Results are within the same range as in plane

y_0 especially when accounting for the standard deviations. The same global behaviour is observed: Γ reduces when x^* increases and the radius r_c^* does not vary significantly. Nevertheless, both metrics are inferior to those in the symmetry plane. It means that weak 3D effects exist although they cannot be more thoroughly investigated with the available database. Structure are then larger and more energetic in the symmetry plane. It appears to be consistent with hairpin vortices centred around the symmetry plane.

Table 3: Lamb-Oseen vortex modelling results.

	Plane A	Plane B	Plane C
Fitted/Total ($y^* = 0$)	38/44	43/45	25/29
$r_c^*(y_0)$	0.68 ± 0.2	0.68 ± 0.2	0.72 ± 0.1
$\Gamma^*(y_0)$	-1.6 ± 0.6	-1.4 ± 0.4	-1.3 ± 0.4
Fitted/Total ($y^* = 1$)	24/30	25/30	25/32
$r_c^*(y_1)$	0.52 ± 0.1	0.51 ± 0.2	0.42 ± 0.1
$\Gamma^*(y_1)$	-1.4 ± 0.5	-1.0 ± 0.3	-0.9 ± 0.4

Most of the vortices whose trajectories are described in Fig.18 have a low rising angle trajectory ($\gamma = 5.3^\circ$) with circular form as shown in Fig.20. The rising velocity $v_{vtx} = \|\vec{v}_z\|/\bar{U}$ is evaluated here at: $v_{vtx} = 0.3$.

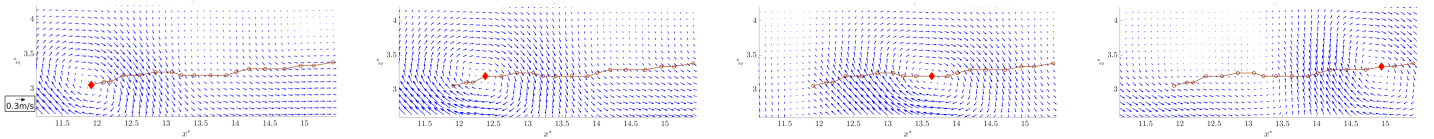


Figure 20: Velocity map of a vortex trajectory with horizontal behaviour between $t = 81.3s$ and $t = 82.4s$ in plane B (y_0).

Otherwise, some of the trajectories are more oriented towards the surface, with a higher rising angle. On Fig.18(b), trajectories with the highest rising angle are highlighted. It appears that these trajectories present a common behaviour: while rising up, the vortex shifts from a circular to an elliptical form. Circulation around it becomes more intense. The vortex dynamic of the yellow trajectory in bold in Fig.18(b) is illustrated in Fig.21. For this example, the rising velocity is $v_{vtx} = 0.8$, more than 2 times the horizontal case, with a rising angle of 16.2° , three times superior. For the nine selected events rising up, averaged results give a radius of 0.64 ± 0.08 and a circulation of -1.7 ± 0.3 . In the previous section, Lamb-Oseen vortex approximation gave in average $r_c^* = 0.68 \pm 0.2$ and $\Gamma^* = -1.4 \pm 0.4$ for

all trajectories in plane B. These results confirm the previous observations. Indeed, as the vortex becomes elliptical its horizontal radius r_c reduces. Hence, rising angle vortices are more energetic and their shape changes as they extend towards the surface rising up in the water column.

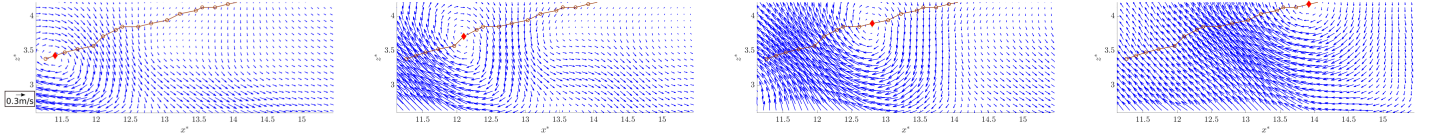


Figure 21: Velocity map of a vortex trajectory rising up between $t = 54.6s$ and $t = 55.1s$ in plane B (y_0).

4.3. Temporal analysis

Using LDV measurements, a spectral analysis is performed in the symmetry plane y_0 . Acquisitions last 6 minutes and frequency varies. For each streamwise position x^* , the lowest average acquisition frequency for each altitude is taken: $f_e(x^* = 7) = 84 Hz$ and $f_e(x^* = 11) = 75 Hz$. Using f_e , LDV signals are re-sampled. Signals are then cut into blocks of 1024 points and a Fast Fourier Transform is applied on every bloc. Power Spectrum Densities are then plotted versus the Strouhal number: $S_t = fH/U_\infty$ in Fig.22 (a) and (b) in the near field. Altitudes are chosen to represent the flow above, under and at the shear layer position. Three different flow behaviours are detected. First: below $z^* = 3$ in $x^* = 7$ and below $z^* = 3.6$ for $x^* = 11$, the energetic content is high since those points are located in the shear layer. Furthermore, a sharp peak is detected for $S_t \simeq 0.062$. Second, there is a transitional part in-between where spectrum do not show any peak. And third, above $z^* = 3.4$ for $x^* = 7$ and above $z^* = 3.6$ for $x^* = 11$, the energetic content is lower and the peak is detected for a higher frequency of $S_t \simeq 0.072$. The higher peak $S_t \simeq 0.072$ is close to the literature for dunes cases in [Omidyeganeh and Piomelli (2011)], it corresponds to the vortex shedding. Periodic events indicated by the lower peak $S_t \simeq 0.062$, happening underneath the shed vortices in the shear layer do not impact the higher altitudes of the water column. Therefore, every event occurring in the top part of the water column must originate from vortices shed from the shear layer. The same results was found by [Omidyeganeh and Piomelli (2011)] that carried out LES simulation on dunes. Fig.22(c) shows the presence of a peak in the far field, close to the surface. That measurement point

is the only one available for $x^* > 11$. The peak is around $S_t = 0.072$ confirming that the events detected above the shear layer are still present at the same frequency close to the surface and they will presumably erupt at the free surface. The peak intensity is lower than the peak close to the obstacle indicating a lower energetic content.

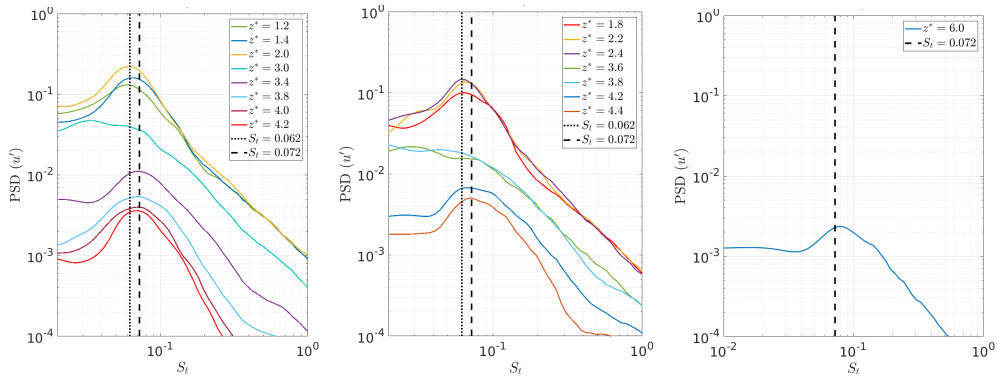


Figure 22: PSD(u') versus $S_t = fH/U_\infty$ in y_0 at $x^* = 7$ (left), $x^* = 11$ (middle) and $x^* = 19$ (right).

In Fig.23, a map of instantaneous $u'w'$ (obtained from PIV measurements) for z^* versus t is plotted for a chosen streamwise position at $x^* = 11$. A vortex passing is detected with a high $u'w' > 0$ peak followed by $u'w' < 0$ with amplitude superior to 0.02. At mid-height ($z^* = 3$), periodic vortex passing is observed. It matches the frequency found in Fig.22 for vortex shedding. The constant shedding of vortices is visible until $z^* = 3.5$ which is the boundary of the shear layer. Some events are more energetic than others and are still persistent above $z^* = 4$, at $t = 40$ s for instance. These highly turbulent events that rise higher are more energetic than others. On Fig.23 and 24, two zones are highlighted. In red, a zone that presents highly turbulent events rising higher than the average turbulent events, they are still visible on the signals at $z^* = 4$. In green, a zone where vortices do not show higher than $z^* = 3.5$.

Instantaneous $u'w'$ signals are plotted in Fig.24 at the same streamwise position: $x^* = 11$ and for two altitudes: $z^* = 3$ and $z^* = 4$ for the 150 s of the PIV acquisition. This figure illustrates what is explained in the previous section: at $z^* = 3$, vortex shedding induces a periodic fluctuating velocity variation. It occurs at the frequency detected in the spectrum in Fig.22(b). At a higher position ($z^* = 4$), although the frequency is still visible on the

spectrum, it does not show on the signals with the used scale. Some intense events are detected. These are the very energetic events that rise higher than the shear layer and they will be assimilated to hairpin structures in the next section.

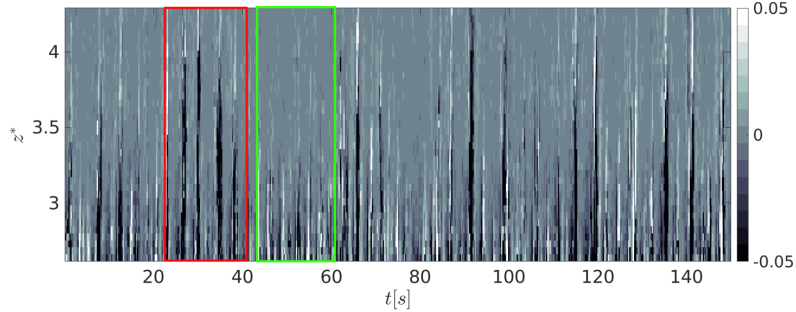


Figure 23: $u'w'$ in a z^* versus t map in y_0 at $x^* = 11$, from PIV measurements.

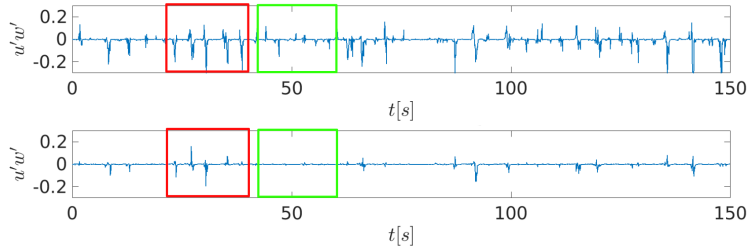


Figure 24: Instantaneous $u'w'$ signals for $(x^* = 11, y^* = 0, z^* = 3)$ (**top**) and $(x^* = 11, y^* = 0, z^* = 4)$ (**bottom**).

4.4. Discussion on detected vortices

Looking at previous results, there seems to be two kinds of structures coexisting in the cylinder wake. The presence of the obstacle in a flow promotes the creation of a shear layer and, as in a mixing layer, Kelvin-Helmholtz instabilities are generated from the velocity difference between the outer flow and the recirculation region underneath. These vortices are detected on the edges of the shear layer, close to the obstacle, which is consistent with Kelvin-Helmholtz instabilities. The shedding frequency is detected in the spectral analysis. Then, as demonstrated in [Müller and Gyr (1987); Leweke et al. (2016)], these events can merge, pair-up or interact to form hairpin structures. It is indeed illustrated by the works of [Diabil et al.

(2017)] and by [Chaurasia and Thompson (2011)], both working on the flow past large plates. Hairpin structures are then more persistent and energetic with a higher rising angle and they are ejected towards the free surface. Structures transverse extension is around $2H = 0.5 m$ and the resulting boils are around $1 m$ wide: it implies that hairpin structures generate boil wider than their width when erupting at the surface [Best (2005a)]. Temporal analysis validates the assumption that these structures are hairpin boil-generating vortices created from Kelvin-Helmholtz vortices interactions in the separated shear layer as detailed by [Müller and Gyr (1987)]. This assumption opposes to hairpin vortices generated underneath the shear layer from near-wall bursts or reattachment flapping conjectures [Kiya and Sasaki (1985); Kadota and Nezu (1999)]. Such explanations are consistent with vortices detected in the PIV measurement planes being 2D sections of a larger 3D event. Furthermore, these events are only visible past large A_R obstacles. Indeed, in previous works [Ikhennicheu et al. (2018a)], it is shown that in the case of low A_R obstacles such as a wall-mounted cube, Kelvin-Helmholtz vortices do not form structures able to rise up to the free surface. It is also explained by [Diabil et al. (2017)] in their numerical study on large and low A_R plates.

5. Conclusion and perspectives

In this study, the flow past a wide wall-mounted square cylinder of aspect ratio $A_R = 6$ is studied. From PIV measurements, the wake past the obstacle is characterized. Key-elements of the wake past the obstacle are identified. Recirculation length in the symmetry plane is $l^* = 6$, it then reduces by 8% in $y1$ and 18% in $y2$. Average Reynolds shear stress maps illustrate the shear layer behaviour, its position is very similar between $y0$ and $y1$ whereas in $y2$ it is redirected towards the floor. The flow behaviour is similar between $y0$ and $y1$ and shows significant differences for $y2$ with the apparition of side effects. At the free surface of the tank, $1 m$ wide boils can be observed. These events originate in the cylinder wake and rise up to the surface. In order to understand these structures behaviour, PIV measurements are filtered using Proper Orthogonal Decomposition. Based on existing methods, a centre detection algorithm is applied. It allows to elucidate vortices trajectories. No vortex is large or energetic enough to be detected in field $y2$. Authors conclude that the transverse extend of the vortex lies between $y0$ and $y1$, hence from $2H$ to $4H$ ($0.5 m$ to $1 m$). In average, rising angle of vortices is $\sim 8^\circ$, which is higher than the shear layer

rising angle of $\sim 4^\circ$. Velocity profiles are fitted with a Lamb-Oseen profiles showing that the vortices radius stays similar with x^* : $\overline{r_c^*} = 0.69$ in y_0 . However circulation reduces with x^* . It is an effect of vortices dissipation. It is then showed that some vortices are impulsed towards the surface. They show a stronger circulation, a larger rising velocity and their shape shifts from a circular to an elliptical form. Finally, a temporal analysis validates that some events rise higher in the water column than others. In the discussion, authors suggest that two phenomena coexist. Kelvin-Helmholtz instabilities develop downstream of the obstacle, in the shear layer, close to the obstacle. Then, these events merge, pair up or interact to form hairpin structures ejected towards the free surface to form large boils. Such boils, that exist at sea can have a major impact on turbines and must be considered in calculations for loads on tidal turbines.

The problem investigated here is also under development from a numerical perspective [Mercier et al. (2017)]. After validation, numerical analysis will offer a 3D understanding of the turbulent phenomenon occurring in the cylinder wake.

Acknowledgment

This work benefits from a French State grant managed by the National Research Agency under the Investments for the Future program bearing the reference ANR-10-IEED-0006-11. The authors also acknowledge the financial support of IFREMER and the Hauts de France Regional Council for this PhD study. We are most grateful to Thomas Bacchetti, Inès Belarbi and Jean-Valery Facq for their assistance and precious advices.

References

- Adrian, R., Meinhart, C., and Tomkins, C. (2000). Vortex organization in the outer region of the turbulent boundary layer. *J. Fluid. Mech*, 422:1–54.
- Adrian, R. and Westerweel, J. (2011). Particle image velocimetry. *Cambridge University Press, Cambridge*.
- Best, J. (2005a). The fluid dynamics of river dunes: A review and some future research directions. *J. Geophys. Res.*, 110.
- Best, J. (2005b). Kinematics, topology and significance of dune-related macroturbulence: some observations from the laboratory and field. *Fluvial sedimentology VII*, 35:41–60.

- Castro, I. (1979). Relaxing wakes behind surface-mounted obstacles in rough wall boundary layers. *J. Fluid. Mech.*, 93:631–659.
- Castro, I. and Robins, A. (1977). The flow around a surface-mounted cube in uniform and turbulent streams. *J. Fluid Mech.*, 79:307–335.
- Chaurasia, H. and Thompson, M. (2011). Three-dimensional instabilities in the boundary-layer flow over a long rectangular plate. *J. Fluid Mech.*, 681:411–433.
- Diabil, H., Li, X., and Abdalla, I. E. (2017). Coherent structures and flow topology of transitional separated-reattached flow over two and three dimensional geometrical shapes. *Mathematical Methods and Computational Techniques in Science and Engineering- AIP Conference proceedings*, 020019.
- Druault, P., Bouhoubeiny, E., and Germain, G. (2012). POD investigation of the unsteady turbulent boundary layer developing over porous moving flexible fishing net structure. *Exp. Fluids*, 53:277–292.
- Druault, P., Guibert, P., and Alizon, F. (2005). Use of proper orthogonal decomposition for time interpolation from PIV data. Application to the cycle-to-cycle variation analysis of in-cylinder engine flows. *Exp. Fluids*, 39:1009–1023.
- Duràn Medina, O., Schmitt, F., Calif, R., Germain, G., and Gaurier, B. (2015). Correlation between synchronised power and flow measurements, a way to characterize turbulent effects on a marine current turbine. *EWTEC, Nantes, France*.
- Duràn Medina, O., Schmitt, F., Calif, R., Germain, G., and Gaurier, B. (2017). Turbulence analysis and multiscale correlations between synchronized flow velocity and marine turbine power production. *Renew. Energ.*, 112:314–327.
- EDF (2010). Énergies marines hydrolienne et houlomotrice. *Conférence institut Coriolis*.
- Graftieaux, L., Michard, M., and Grosjean, N. (2001). Combining PIV, POD and vortex identification algorithms for the study of unsteady turbulent swirling flows. *Meas. Sci. Technol.*, 12:1422–1429.

- Hamed, A., Pagan-Vazquez, A., Khovalyg, D., Zhang, Z., and Chamorro, L. (2017). Vortical structures in the near wake of tabs with various geometries. *J. Fluid Mech.*, 825:167–188.
- Hearst, R. J., Gomit, G., and Ganapathisubramani, B. (2016). Effect of turbulence on the wake of a wall-mounted cube. *J. Fluid Mech.*, 804:513–530.
- Ikhennicheu, M., Gaurier, B., Druault, P., and Germain, G. (2018a). Experimental analysis of the floor inclination effect on the turbulent wake developing behind a wall mounted cube. *Eur. J. Mech. B/Fluid*, 72:340–352.
- Ikhennicheu, M., Germain, G., Gaurier, B., and Druault, P. (2018b). Experimental study of the wake past cubic wall-mounted elements to predict flow variations for tidal turbines. *AWTEC, Taipei, Taiwan*.
- Kadota, A. and Nezu, I. (1999). Three-dimensional structure of space-time correlation on coherent vortices generated behind dune crest. *J. Hydraul. Eng.*, 37:59–80.
- Kiya, M. and Sasaki, K. (1985). Structures of large-scale vortices and unsteady reverse flow in the reattaching zone of a turbulent separation bubble. *J. Fluid Mech.*, 154:463–491.
- Leweke, T., Le Dizès, S., and Williamson, C. (2016). Dynamics and instabilities of vortex pairs. *Annu. Rev. Fluid Mech.*, 37:59–80.
- Lim, H., Castro, I., and Hoxey, R. (2007). Bluff bodies in deep turbulent boundary layers: Reynolds-number issues. *J. Fluid Mech.*, 570:97–118.
- Liu, Y., Ke, F., and Sung, H. (2008). Unsteady separated and reattaching turbulent flow over a two-dimensional square rib. *J. Fluid Struct.*, 24:366–381.
- Lumley, J. (1967). The structure of inhomogeneous turbulent flows. *A.M. Yaglom, V.I. Tararsky (Eds.), Atmospheric Turbulence and Radio Wave Propagation*.
- Martinuzzi, R. and Tropea, C. (1993). The flow around surface-mounted, prismatic obstacles placed in a fully developed channel flow, (*Data Bank Contribution*). *J. Fluid Eng.*, 115:85–92.

- Meinhart, C., Prasad, A., and Adrian, R. (1993). A parallel digital processor system for particle image velocimetry. *Meas. Sci. Technol.*, 4:619–626.
- Mercier, M., Grondeau, M., Guillou, S., Thiébot, J., and Poizot, E. (2017). Towards the modelling of turbulence at tidal stream power sites with the lattice boltzmann method. *EWTEC, Cork, Ireland*.
- Moriconi, L. (2009). Minimalist turbulent boundary layer model. *Phys. Rev.*, 79:046306.
- Müller, A. and Gyr, A. (1987). On the vortex formation in the mixing layer behind dunes. *J. Hydraul. Res.*, 24:359–375.
- Mycek, P., Gaurier, B., Germain, G., Pinon, G., and Rivolaen, E. (2014). Experimental study of the turbulence intensity effects on marine current turbines behaviour. Part I: One single turbine. *Renew. Energ.*, 66:729–746.
- Myers, L. and Bahaj, A. (2005). Simulated electrical power potential harnessed by marine current turbine arrays in the alderney race. *Renew. Energ.*, 30:1713–1731.
- Omidyeganeh, M. and Piomelli, U. (2011). Large-eddy simulation of two-dimensional dunes in a steady, unidirectional flow. *J. Turbul.*, 42:1–31.
- Panigrahi, P. and Acharya, S. (2004). Multi-modal forcing of the separated shear flow past a rib. *J. Fluid Eng.*, 126:22–31.
- Sabatino, D. and Rossmann, T. (2016). Tomographic PIV measurements of a regenerating hairpin vortex. *Exp. Fluids*, 57:6.
- Sattari, P., Bourgeois, J., and Martinuzzi, R. (2012). On the vortex dynamics in the wake of a finite surface-mounted square cylinder. *Exp. Fluids*, 52:1149–1167.
- Schofield, W. and Logan, E. (1990). Turbulent shear flow over surface mounted obstacles. *J. Fluid Eng.*, 112:376–385.
- SHOM (2015). MNT bathymétrie de façade atlantique (projet homonim).
- Sirovich, L. (1987). Turbulence and the dynamics of coherent structures. Part I: Coherent structures. *Q Appl. Math.*, XLV:561–571.

- Volino, R., Schultz, M., and Flack, K. (2009). Turbulence structure in a boundary layer with two-dimensional roughness. *J. Fluid Mech.*, 635:75–101.
- Wang, L., Salewski, M., and Sundén, B. (2009). Turbulent flow in a ribbed channel: Flow structures in the vicinity of a rib. *Exp. Therm. Fluid Sci.*, 34(2):165–176.
- Westerweel, J. and Scarano, F. (2005). Universal outlier detection for PIV data. *Exp. Fluids*, 39:1096–1100.